

Article

Influence of Ceramic Particles Character on Resulted Properties of Zinc-Hydroxyapatite/Monetite Composites

Klára Hosová ¹, Jan Pinc ^{1,2,*}, Andrea Školáková ², Vilém Bartůněk ³, Petr Veřtát ², Tereza Školáková ⁴, Filip Průša ¹, Dalibor Vojtěch ¹ and Jaroslav Čapek ²

- ¹ Department of Metals and Corrosion Engineering, Faculty of Chemical Technology, University of Chemistry and Technology, Prague, Technická 5, 166 28 Prague 6, Czech Republic; hosovak@vscht.cz (K.H.); prusaf@vscht.cz (F.P.); vojtechd@vscht.cz (D.V.)
- ² Institute of Physics of the Czech Academy of Sciences, Na Slovance 1999/2, 182 21 Prague 8, Czech Republic; skolakova@fzu.cz (A.Š.); vertat@fzu.cz (P.V.); capekj@fzu.cz (J.Č.)
- ³ Department of Inorganic Chemistry, Faculty of Chemical Technology, University of Chemistry and Technology, Prague, Technická 5, 166 28 Praha 6, Czech Republic; bartunev@vscht.cz
- ⁴ Department of Organic Technology, Faculty of Chemical Technology, University of Chemistry and Technology, Prague, Technická 5, 166 28 Prague 6, Czech Republic; skolakot@vscht.cz
- * Correspondence: pinc@fzu.cz; Tel.: +420-266-05-2631



Citation: Hosová, K.; Pinc, J.; Školáková, A.; Bartůněk, V.; Veřtát, P.; Školáková, T.; Průša, F.; Vojtěch, D.; Čapek, J. Influence of Ceramic Particles Character on Resulted Properties of Zinc-Hydroxyapatite/Monetite Composites. *Metals* **2021**, *11*, 499. <https://doi.org/10.3390/met11030499>

Academic Editors: Changdong Gua and Daolun Chen

Received: 27 February 2021

Accepted: 15 March 2021

Published: 17 March 2021

Publisher's Note: MDPI stays neutral with regard to jurisdictional claims in published maps and institutional affiliations.



Copyright: © 2021 by the authors. Licensee MDPI, Basel, Switzerland. This article is an open access article distributed under the terms and conditions of the Creative Commons Attribution (CC BY) license (<https://creativecommons.org/licenses/by/4.0/>).

Abstract: Zinc and its alloys seem to be promising candidates for biodegradable applications. Those materials are often modified by other elements or compounds in order to enhance their properties. The combination of zinc and apatites is challenging for several reasons. However, the advantages connected with the biological aspects suggest the need for further research into such materials. In this study, three zinc-based composites with 4 and 8 wt. % of nanohydroxyapatite or nanomonetite (Zn-4MO, Zn-4HA, Zn-8HA) were prepared by sintering and subsequent extrusion. Materials prepared in this way were characterized from the microstructural, mechanical and corrosion point of view. The obtained results showed a significant influence of particle character (amount and morphology) on the strength and ductility of the prepared materials. In case of Zn-4MO, the presence of monetite significantly increased the ductility compared with the other materials. In addition, the increment of the degradation rate caused by the presence of monetite was observed as well. All obtained results pointed out to significant advantages of monetite for the preparation of Zn-apatite composites compared with hydroxyapatite.

Keywords: biodegradable material; zinc; hydroxyapatite; monetite; metal-matrix composites

1. Introduction

Biodegradable metals are attractive materials for biomedical applications due to their beneficial ability to slowly degrade under physiological conditions [1–3]. For this reason, there is no need to reoperate on a patient to remove an implant, which has fulfilled its function and its present in the human body is no further essential. Obviously, the material and its corrosion products must not cause any adverse effects to human organisms [4]. Simultaneously, the material should be able to mimic the replaced tissue from all aspects of medical requirements (structure, mechanical properties, interaction with surrounding tissue, etc.) [5,6]. Until now, the mentioned requirements were partially accomplished by iron [7,8], magnesium [9,10] and zinc-based [11,12] materials.

Zinc-based materials are in the center of attention predominantly due to their impressive material properties related to biodegradable applications [13–16]. These materials are chosen as suitable representatives because of almost ideal corrosion behavior under the simulated body conditions [17]. The materials degrade with an acceptable rate, and the hydrogen gas is not evolved during its exposition (oxygen depolarization reaction [18]). Despite its proper corrosion behavior, there were still problems concerning mechanical

performance. However, those problems have recently been overcome efficiently by alloying. The most promising alloying proved to be of Sr [19], Mn [20], Li [21], Mg [22], Fe [23], Ag [24] and their combinations [23,25–29]. The last obstacle is relatively poor cell adhesion to the material surface, which is evident during direct *in vitro* testing [30]. Cell adhesion is a crucial parameter for the proliferation or synthesis of matrix proteins [31]. Besides, it affects a large group of properties closely associated with the material degradation process [4,22]. The aforementioned facts pointed to the importance of this parameter, even in the case of biodegradable materials which gradually dissolve in the organism.

One of the possible approaches for solving such shortcomings is the combination of zinc with materials enhancing the implant–cell interaction [32]. This enhancement is often achieved by using components already occurring in the human body. However, the selection of suitable compounds is restricted by several criteria (thermal stability, mechanical properties, etc.), which affect the processing as well as the resulting behavior of the composite material [33]. The mentioned criteria are accomplished predominantly by inorganic compounds forming human bone, such as hydroxyapatite, tricalcium phosphate or their derivatives [34–36]. It is well known that the presence of those substances significantly improves bioactivity and cell proliferation [37,38]. Based on that, the combination of Zn with hydroxyapatite and other similar compounds seems to be a suitable approach to obtain the desired improvement of the Zn matrix composites for biodegradable applications. To the best of our knowledge, only a few studies concerning the preparation and characterization of zinc-hydroxyapatite (Zn-HA) composites have been published [39–42]. The authors confirmed the potential of these materials to be used as biodegradable materials, especially from the corrosion and the *in vitro* and *in vivo* points of view. Besides, the gradual increment of the hydroxyapatite content leads to a decrease in the composite mechanical properties, compared with pure zinc [42,43]. This decrease is often caused by the absence of an efficient bond between the matrix and the reinforcement. Due to this, there have been efforts to enhance the connection using thermomechanical processing [40] or using other components (iron) [41], which should improve the overall performance of the obtained materials. However, the enhancement was not reached by those methods and it still belongs to the challenge, which must be solved before the effective usage of Zn-HA composites.

In this study, the zinc-based composites prepared by a combination of spark plasma sintering and extrusion were characterized. Until now, the mechanical properties of Zn-HA composites have always been worse compared with pure zinc for several reasons. In our study, we reached mechanical properties comparable with those for pure zinc by modification of particle parameters of non-metallic components (size, shape and their content in the composite structure). Besides, the influence of those parameters on overall material performance was studied as well. This study paves the way to a significant enhancement of mechanical properties and increases the potential usability of those materials as biodegradable implants.

2. Materials and Methods

2.1. Powder Characterization and Preparation of Powder Mixtures

The specimens were prepared using powders of pure zinc (Zn, Alfa Aesar, -140 + 325 mesh, 99.9%, metals basis), hydroxyapatite (HA, Sigma-Aldrich, <200 nm particle size, ≥97%, synthetic) and monetite (MO, reported in work [44]). Nanopowders (HA, MO) were characterized using transmission electron microscope EFTEM Jeol 2200 FS (TEM, Jeol Ltd., Tokyo, Japan) and the basic characterization of the powders (particles size, shape, etc.) was done by image analysis using ImageJ software (v.1.53e, Wayne Rasband and National Institutes of Health, MD, USA). Particle size distributions (PSDs) of hydroxyapatite and monetite nanoparticles were analyzed by laser diffraction method using Malvern Mastersizer 3000 device (Malvern Instruments Ltd., Malvern, UK) equipped with Hydro MV medium volume unit (Malvern Instruments Ltd., Malvern, UK). The conditions of measurement were optimized for each of the materials to ensure the dispersion of material.

An adequate amount of sample, i.e., at an obscuration range of 5–15%, was added into the wet unit with a set stirring speed and sonication (3000 rpm and ultrasound at 20% for hydroxyapatite, 3500 rpm and ultrasound at 10% for monetite). The refractive index for hydroxyapatite and monetite was 1.644 and 1.5870, respectively. The measurements were carried out in water as a dispersion medium. The materials were measured three times and the PSD was determined from the average values. PSD was also characterized by d-values (d10, d50 and d90), which are generally used as the acceptance criteria. These parameters relate to the cumulative size distribution at 10%, 50%, or 90%, representing a certain size of particles below which 10%, 50%, or 90% of the sample lies. Zinc powder was mixed with 4 and 8 wt. % of HA (8.8 vol. %, Zn-4HA; 16.7 vol. %, Zn-8HA) or 4 wt. % of MO (9.2 vol. %, Zn-4MO), and the resulted mixtures were homogenized using two different methods. The level of homogenization was observed by the eye and subsequently using scanning electron microscopy (SEM, Tescan Vega, Brno, Czech Republic) equipped with an energy-dispersive spectrometer (EDS, Oxford Instruments, 20 mm², High Wycombe, United Kingdom). First of all, both powder mixtures were homogenized using a conventional tumbling Turbula mixer (T2F model, W.A. Bachofen, Basel, Switzerland) at 50 rpm for a 20 min period. However, this method led only to the homogenization of the Zn-4MO sample. In the case of the Zn-4HA sample, different conditions of mixing were done (2 × 20 min 50 rpm, 20 min 75 rpm, 60 min 75 rpm); however, the homogeneity of the mixture was not reached using this method. Experimentally, the areas with concentrated white powder were visible on top of the Zn-4HA and Zn-8HA mixtures. Based on these results, the Zn-HA powder mixtures were homogenized in mortar. This homogenization process took approximately 2 min using minimal force to avoid deformation of zinc particles.

2.2. Thermomechanical Processing

Homogenized powder mixtures were compacted using spark plasma sintering (SPS, FCT Systeme HP-D 10, Rauenstein, Germany) with a characteristic setup to ensure the best compactness of the resulted materials. Approximately 30 g of homogenized mixture was used per one tablet and the whole process was performed in a vacuum. In the initial stages of processing, the mixture was heated up to 260 °C with a slow increment of the temperature (20% power) due to removal of redundant moisture from the powder mixture. Subsequently, the sample was heated to 380 °C with a heating speed of 10 °C/min. After reaching 380 °C, the mixture was pressed using a 10 kN force and remained compressed for a 10 min period. Samples were then cooled with a maximal cooling speed of the machine while relieving the compaction force during a 5 min cooling segment to minimize the activity of recrystallization processes. The prepared samples with 20 mm in diameter prepared by SPS process were then extruded at 300 °C using a hydraulic press. Before the process itself, the samples were tempered for 10 min in the extrusion die and subsequently extruded with using an extrusion ratio 10:1 (20 → 6 mm). High-temperature paste Gleit-μ HP 505 was used as a lubricant during the process and the ram speed was set to 0.2 mm/s. Immediately after the process, the samples were cooled by water in order to avoid the static recrystallization process. Materials prepared in this route were machined for the microstructural, mechanical and corrosion measurements by turning.

2.3. Microstructure

The microstructure of the extruded samples was observed in the extrusion direction (ED) and the direction perpendicular to ED (PD). The samples were ground using P80–P4000 sandpapers and subsequently electrochemically polished in a H₃PO₄: ethanol (volume 50:50) solution using stainless steel as a counter electrode (−15 °C, 10 min, 4 V). For the microstructural observations, an optical microscope Nikon MA 200 (Nikon, Minato, Tokyo, Japan) and a FEI 3D Quanta 3D field-emission-gun DualBeam microscope (Thermo Fisher Scientific, Waltham, MA, USA) equipped with an electron back scatter diffraction detector TSL/EDAX Hikari (EBSD, Ametek, Berwyn, IL, USA) were used. Texture, grain size and the inverse pole figure maps were analyzed using EDAX OIM Analysis v8 soft-

ware (Version 8.0, Amatek, Berwyn, IL, USA). Besides, the porosity of the materials was determined using calculations according to Equations (1) and (2).

$$\varepsilon_{\text{theoretical}} = \left(1 - \frac{\rho_{\text{real}}}{\rho_{\text{theoretical}}}\right) \cdot 100 \quad (1)$$

where $\varepsilon_{\text{theoretical}}$ is the theoretical porosity of the sample, ρ_{real} is the density calculated from the sample dimensions and weight, $\rho_{\text{theoretical}}$ is the density obtained by Equation (2).

$$\rho_{\text{theoretical}} = \rho_{\text{Zn}} \cdot w_{\text{Zn}} + \rho_X \cdot w_X \quad (2)$$

where $\rho_{\text{Zn}} = 7.14 \text{ g/cm}^3$, X is the index for ceramic components ($\rho_{\text{HA}} = 3.08 \text{ g/cm}^3$, $\rho_{\text{MO}} = 2.92 \text{ g/cm}^3$), w is the mass fraction of the individual components.

2.4. Mechanical Properties

Compressive and tensile measurements were used for the evaluation of mechanical behavior of the prepared materials. All those measurements were done in ED at an ambient temperature using an INSTRON 5882 universal testing machine (Instron, Wien, Austria) equipped with an Instron Dynamic Extensometer (gauge length of 12.5 mm). Compressive tests were performed on the cuboid samples with a side length of 5 mm and a high of 7.5 mm. During the compressive measurement, the ram speed was set to 0.45 mm/min, and the testing was done according to ASTM E9-19 standard. Tensile properties were measured using cylindrical samples with a gauge length of 15 mm, 4 mm in diameter and a ram speed of 0.9 mm/min. Tensile testing was performed according to ASTM E8/E8M-16a Standard. In both cases (compressive and tensile testing), three samples were always used for the measurements to provide a sufficient statistical data set. Vickers hardness was measured in ED and PD with a load of 1 kg.

2.5. Corrosion Tests

Corrosion properties of the prepared materials were studied using immersion tests. Immersion tests were performed in simulated body fluid (SBF27, Table 1) at 37 °C for 14 days. Besides, changes of pH values were systematically measured every second day of the exposition, and the stable ratio between exposed surface area and SBF was set to 80 mL/cm². Cylindrical samples with a height of 7.5 mm and a diameter of 5 mm were turned and subsequently exposed to SBF in plastic containers. After the exposition, the samples were carefully rinsed by ethanol and investigated using stereomicroscope Olympus SZX10 (Olympus, Shinjuku, Tokyo, Japan), SEM-EDS and X-ray diffractometer PANalytical X'Pert Pro equipped with a Co K α source (XRD, Malvern, Worcestershire, UK). Subsequently, the corrosion products were removed chemically using CrO₃ solution (200 g CrO₃/L) and weighted in order to calculate the corrosion rate according to Equation (3) (ASTM G31-72) [45].

$$v_{\text{cor}} = \frac{\Delta m}{t \cdot S \cdot \rho} \quad (3)$$

where Δm is the sample weight loss after immersion, t is the time of immersion, S is the sample area, ρ is the density of the material. Solutions were acidified using nitric acid after the exposition and analyzed using atomic absorption spectroscopy Agilent 280FS AA (AAS, Agilent Technologies, Santa Clara, CA, USA).

Table 1. Composition of SBF27 solution, data from Müller, L. et al. [46].

Ions	c (mmol/L)
Na ⁺	142.0
K ⁺	5.0
Ca ²⁺	2.5
Mg ²⁺	1.0
Cl ⁻	109.0
HCO ³⁻	27.0
SO ₄ ²⁻	1.0
HPO ₄ ²⁻	1.0

3. Results

3.1. Microstructure

The characterization of the initial powders was already studied in our previous works [40,42]. Due to this, only a brief characterization concerning HA and MO nanoparticles is presented in this paper. HA powder consisted of globular particles with an average size 43 ± 20 nm. On the contrary, the MO particles possessed a rod-like shape with the base slightly under 100 nm and a length approximately 300 nm. It is obvious from Figure 1 that there was a difference between particle shape and size but also in the level of particle conglomeration. According to TEM images, the level of conglomeration was in the case of MO (Figure 1b) and was significantly higher in comparison to globular HA (Figure 1a). The conglomeration could be also observed from the results of the analysis of particle size distribution (Figure 1c,d). The particle size distribution of nanoparticles was used to evaluate the relative amount of particles present according to their size. The particle size and particle size distribution was measured by laser diffraction, which is an effective technique for such measuring [47]. As can be seen, the obtained distribution curves are of a bimodal dependence (Figure 1c,d) suggesting the formation of conglomerates. Therefore, the particle distribution size comprises the size of individual conglomerates. Although it could be seemed that the MO nanoparticles are larger according to TEM images (Figure 1a,b), the distribution d50 belonging to HA and MO nanoparticles show the opposite results (Table 2). The 50% of MO conglomerates possessed a size lower than 2.74 μm while the d50 of HA conglomerates was smaller than 3.36 μm .

Table 2. Particle size distribution of nanoparticles.

Nanoparticles	d10 (μm)	d50 (μm)	d90 (μm)
MO	0.74	2.74	6.45
HA	0.22	3.36	11.70

The micrographs of the homogenized mixtures are shown in Figure 2. Despite different methods of mixing (see the Materials and Methods), the nanoparticles occupied predominantly the pits localized on the Zn particles and formed obvious conglomerates of HA and MO in all cases. The detailed observations also confirmed the increment of the conglomerate size after mixing in comparison to the initial state of the particles. It can be also seen from Figure 2b,c that the processing in mortar did not lead to the shape deformation of the Zn particles. Besides, the distribution of HA (Zn-4HA, Zn-8HA) seemed to be more uniform in comparison to the Zn-4MO sample. Distribution of ceramic particles and phase composition of mixed powders were analyzed using EDS and XRD, and the resulted phase quantification (XRD) is summarized in Table 3.

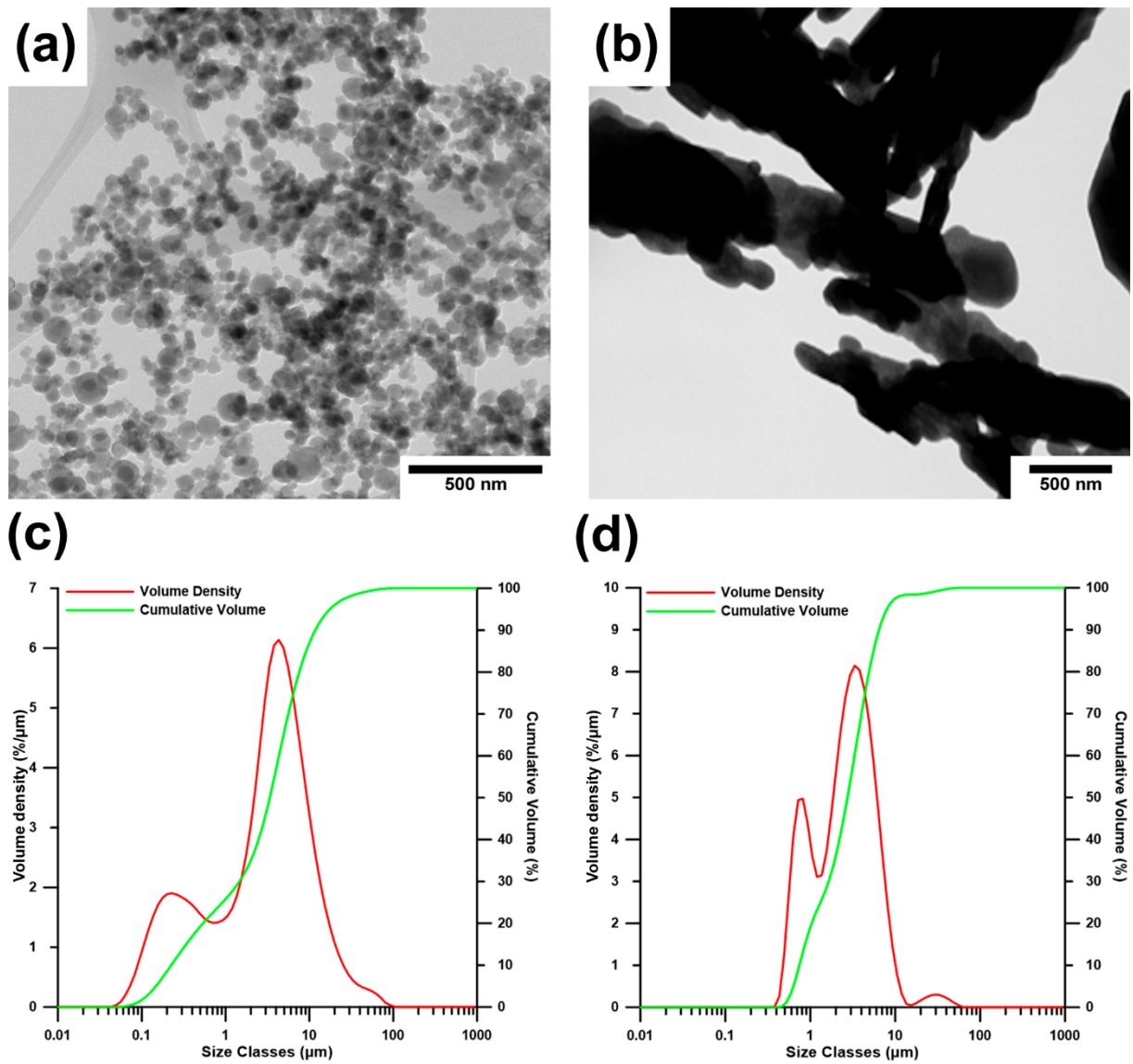


Figure 1. The morphology and distribution curves of (a,c) HA and (b,d) MO particles.

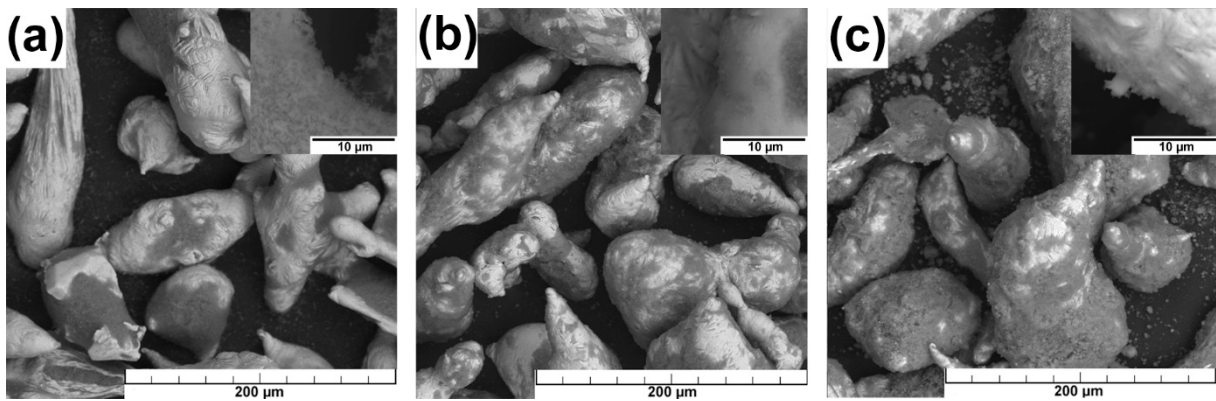


Figure 2. Morphology of (a) Zn-4MO, (b) Zn-4HA and (c) Zn-8HA mixtures after the homogenization process.

Table 3. Phase composition of the powder mixtures according to XRD.

Powder	Mineral	Chemical Formula	SemiQuant (%)
Zn-4MO	Zinc	Zn	86
	Monetite	Ca(PO ₃ OH)	14
Zn-4HA	Zinc	Zn	≥85
	Hydroxyapatite	Ca ₅ (PO ₄) ₃ (OH)	≥15
Zn-8HA	Zinc	Zn	≥80
	Hydroxyapatite	Ca ₅ (PO ₄) ₃ (OH)	≥20

The microstructure and texture of the extruded materials are shown in Figure 3. According to the micrographs (Figure 3a–c), the materials possessed the characteristic alignment of the particles in the extrusion direction. Moreover, the sphere-like conglomerates were visible in the material microstructure. Those conglomerates consisted of ceramic particles (MO, HA) and affected the microstructure of the obtained materials. It can be seen in Figure 3a₁–c₁ that the aforementioned affection of the microstructure was caused by the preferential nucleation of new grains at the interface between zinc and the ceramic particles. Despite this, the average grain size was for all materials approximately the same and reached the value of 10 μm. As can be seen from the inverse pole figures (IPF), slight differences in the texture intensity could be observed between individual samples. Generally, the materials possessed the basal texture with the <10–10> crystallographic directions almost parallel with ED. The intensity of the basal texture decreased with the increasing amount of the ceramic component. On the other hand, the alignment of <10–10> crystallographic directions showed an opposite trend (Figure 3a₂–c₂). In addition, the Kernel average misorientation analysis (KAM) revealed minimal signs of internal stresses in the materials and the low content of low-angle boundaries. Material porosity was calculated according to Equations (1) and (2) and the results are shown in Table 4. These results confirmed the increase of the porosity with the increasing content of ceramic particles.

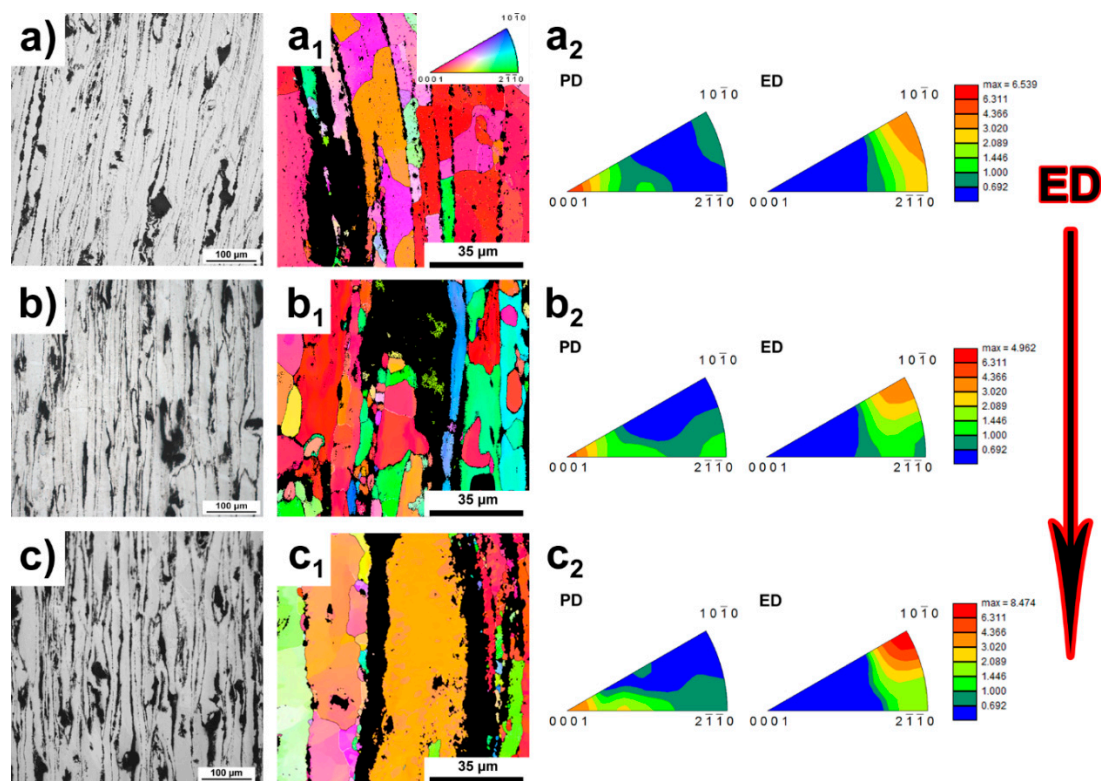


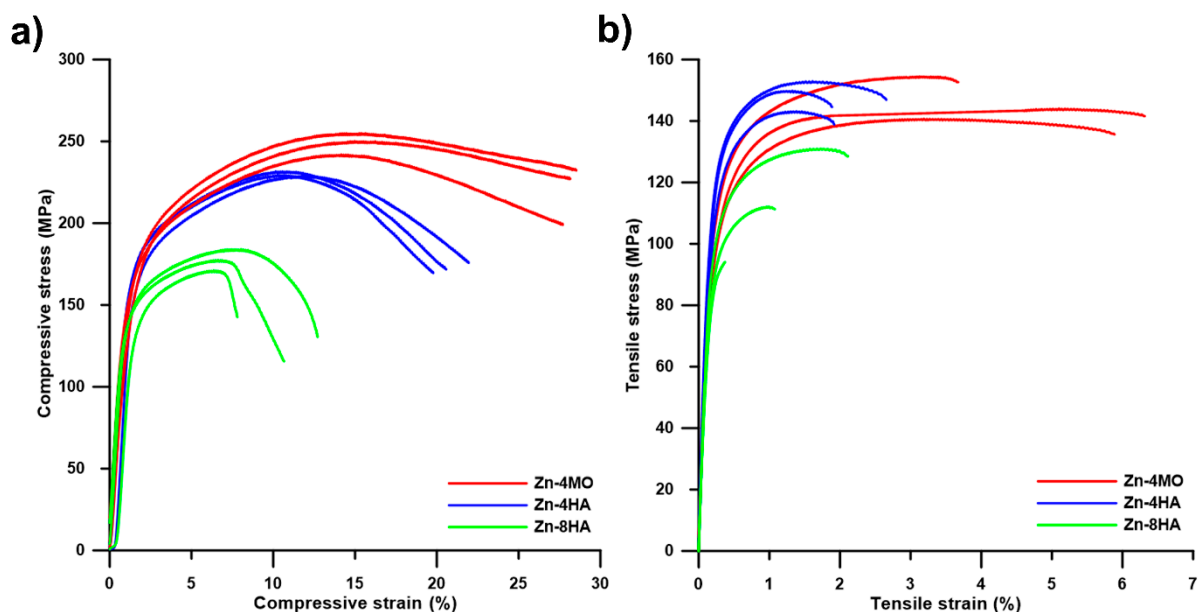
Figure 3. Microstructure (a–c), inverse pole figure maps (a₁–c₁) and IPF (a₂–c₂) of extruded (a) Zn-4MO, (b) Zn-4HA and (c) Zn-8HA. The black spots (in IPF unindexed points) characterize the ceramic particles.

Table 4. Theoretical porosity of the materials.

Sample	Zn-4MO	Zn-4HA	Zn-8HA
Average	8.6%	7.6%	13.7%
Standard deviation	0.6%	0.8%	0.8%

3.2. Mechanical Properties

The mechanical behavior of zinc composites with different contents of ceramic components and particle morphology is shown in Figure 4. The exact measurement values are in Table 5. Compressive tests revealed that higher amount of HA (8 wt. %) led to a decrease in ultimate compressive strength (UCS) approximately by 53 MPa in comparison with Zn-4HA, which possessed the UCS of 229 ± 1 MPa. The best results were obtained in the case of Zn-4MO, where the compressive yield strength (CYS) and UCS reached 146 ± 4 MPa and 249 ± 5 MPa, respectively. Interestingly, the values obtained by tensile tests showed a different trend (Figure 4b). In this case, the Zn-4HA possessed the highest average values of tensile yield strength (TYS, 131 ± 4 MPa) as well as ultimate tensile strength (UTS, 149 ± 4 MPa). However, the difference in those values was negligible between Zn-4HA and Zn-4MO. On the contrary, the ductility value was approximately two times higher in the case of Zn-4MO sample and the values were $5.3 \pm 1.1\%$, $2.1 \pm 0.3\%$, $0.8 \pm 0.4\%$ for Zn-4MO, Zn-4HA and Zn-8HA, respectively. In addition, Young's moduli were determined as the slope of the elastic region of the tensile curves, and the values of modulus were approximately 58 ± 5 GPa for all the studied materials. Finally, the hardness measurement did not confirm the significant changes in its values between the materials. The Vickers hardness value was equal to 42 ± 2 HV1 for all the measured samples.

**Figure 4.** Engineering stress-strain curves obtained by (a) compressive and (b) tensile measurements of zinc composites.**Table 5.** Summary of the compressive and tensile characteristics.

Sample	CYS (MPa)	UCS (MPa)	TYS (MPa)	UTS (MPa)
Zn-4MO	146 ± 4	249 ± 5	117 ± 4	146 ± 6
Zn-4HA	151 ± 1	229 ± 1	131 ± 4	149 ± 4
Zn-8HA	129 ± 2	176 ± 6	101 ± 7	113 ± 15

The fracture surfaces of the Zn-4MO and Zn-4HA composites are shown in Figure 5a,b. In the case of Zn-4HA (Figure 5a), the signs of both cleavage and ductile fractures were observed, suggesting the mixed character. The portion of the signs of plastic deformation (dimples) was significantly smaller in comparison to the proportion of the cleavage fracture (facets). On the contrary, the contribution of plastic deformation was significantly higher in the case of Zn-4MO composite, and the facets were approximately two times larger compared with Zn-4HA (Figure 5b). It was clearly visible from the micrographs that the fracture spread differently in both studied composites. On one hand, the fracture propagated predominantly on the interfaces between Zn particles in the Zn-4HA composite (interparticle propagation); while the fracture spread also through the Zn particles in the Zn-4MO (trans/interparticle propagation). Besides, the rounded conglomerates containing a higher concentration of ceramic particles were observed on the fracture surface in all samples. For these reasons, the differences in mechanical behavior, especially in plasticity, could be ascribed to the distribution of those ceramic particles, their shapes, and their characters.

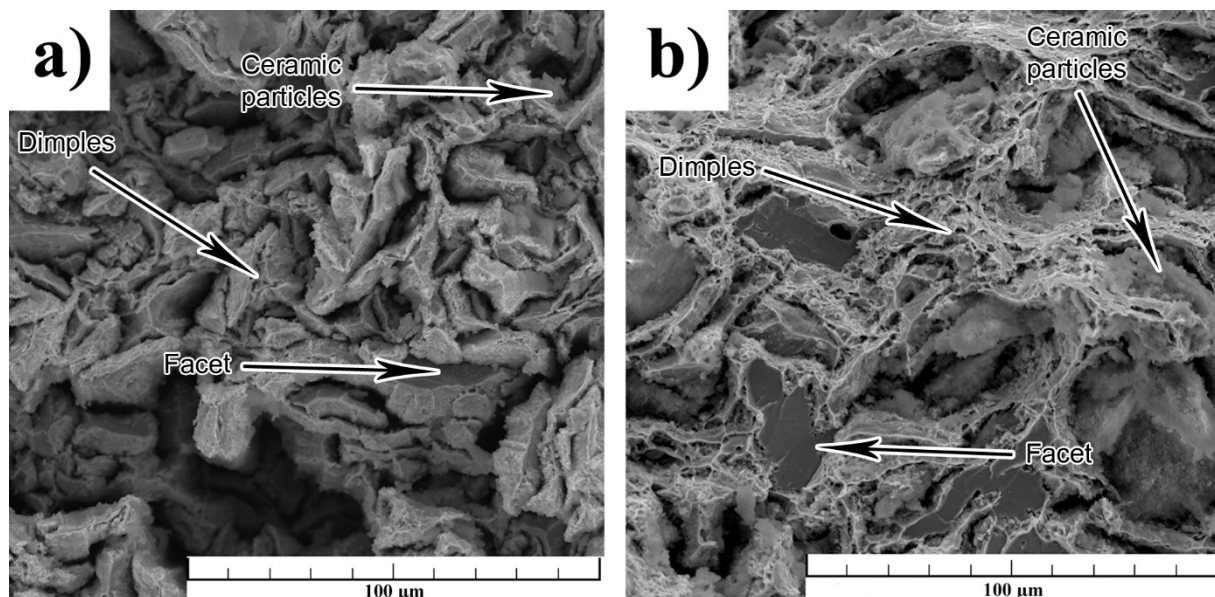


Figure 5. Fracture surfaces of (a) Zn-4HA and (b) Zn-4MO after the tensile measurements.

3.3. Immersion Tests

The corrosion products formed on the material surface after 14 days of exposition in SBF were analyzed using an optical microscope, SEM-EDS, and XRD. Besides, the change in the pH of the corrosion medium was recorded during the experiment and the corrosion rate was determined using weight loss method and the ion release by AAS, respectively. The microscope observations confirmed non-uniform distribution of the corrosion products across the material surfaces. The sample-holder contact area did not affect the obtained results (Figure 6). On the one hand, massive corrosion products formed relatively deep pits (Figure 6a₃–c₃); on the other hand, the regions with processing residues (minimal corrosion attack) were observed on the surface of all tested samples. A higher magnification with the combination of EDS and XRD analyses confirmed the similar morphology and composition of the corrosion products. According to XRD, the major part of the corrosion products found on all investigated materials was formed by hydrozincite (74–82%, $Zn_5(CO_3)_2(OH)_6$). Besides, the presence of simonkolleite (up to 14%, $Zn_5Cl_2(OH)_8 \cdot H_2O$) and zinc hydrogen phosphate (up to 8%, $ZnHPO_4$) were found as well. Localization of the corrosion attack was clearly visible after the pickling.

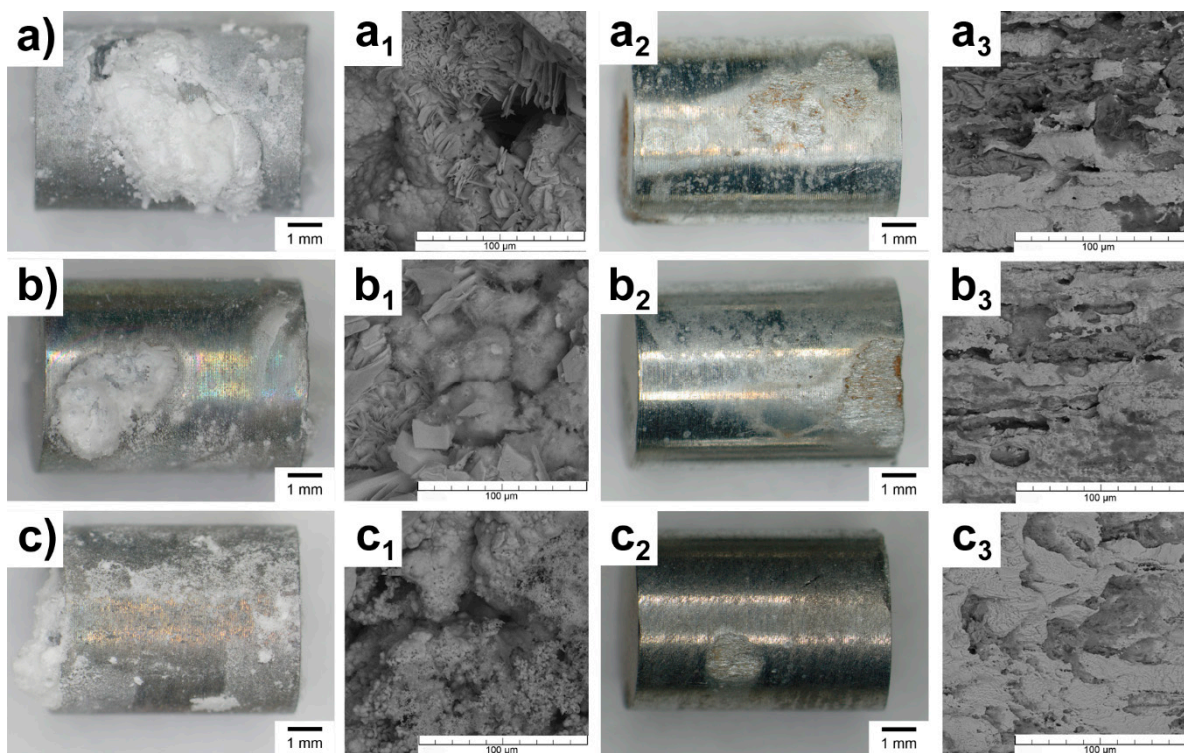


Figure 6. Surface morphology of (a) Zn-4MO, (b) Zn-4HA and (c) Zn-8HA samples after the exposition (a_1 – c_1) in SBF and after the chemical removing of corrosion products (a_2 – c_3).

Weight loss (corrosion rate respectively) was the highest in the case of the Zn-4MO sample, while the lowest values possessed a Zn-8HA sample. In addition, ion release measurements showed the same trend in the corrosion rates (Zn-4MO > Zn-4HA > Zn-8HA); however, the values of corrosion rates were significantly lower. The exact values of weight loss and corrosion rates were determined by the two methods listed in Table 6.

Table 6. Corrosion rates of the composites evaluated by weight loss and ion release.

Sample	Weight Loss (mg)	Corrosion Rate Determined through the Weight Loss		AAS (Zn^{2+}) (mg/L)	Corrosion Rate Determined from the AAS (Zn^{2+}) (mg/cm ² /Day)
		(mm/a)	(mg/cm ² /Day)		
Zn-4MO	12.2 ± 0.4	0.26 ± 0.02	0.51 ± 0.02	15.0 ± 5.6	0.09 ± 0.03
Zn-4HA	7.6 ± 0.9	0.18 ± 0.02	0.35 ± 0.04	15.0 ± 6.4	0.09 ± 0.04
Zn-8HA	3.9 ± 0.2	0.10 ± 0.01	0.19 ± 0.01	11.5 ± 3.7	0.06 ± 0.03

4. Discussion

Characterization of the nanoparticles revealed their willingness to form conglomerates during PSD measurements. The conglomeration process was characterized by a bimodal distribution with sizes in the μm range, while the sizes of the nanoparticles determined by image analyses confirm the nm dimensions of the particles. The same behavior was also observed after the powder homogenization process (Figure 2), where the nanoparticles formed the conglomerates on the surface of zinc particles. Moreover, the rounded conglomerates with a size up to 20 μm were present in the material structure even after the extrusion process. The conglomerates formed by this process had no effective bonds between individual nanoparticles and zinc matrix (insufficient extrusion temperature) resulting in lower cohesion and thus in the decrement of mechanical properties. This pointed out the importance of the process in understanding how to enhance the properties and usability of those materials for biodegradable applications. One of the possible explanations for the

conglomeration process is hidden in the particle size and physical properties of HA and MO nanoparticles. Particle size affects the distribution of the electrical charge on its surface and the mutual electrical interactions between individual particles [48]. This can lead to the formation of conglomerates of different sizes and shapes. Bystrov et al. [48] revealed that the process of HAglomeration is significantly influenced by dipole moment and the number of saturated hydrogen bonds, respectively. With a higher number of saturated hydrogen bonds, the particles form conglomerates with a hexagonal orientation resulting in spherical conglomerates. As can be seen in Figure 2, the conglomerates formed similarly shaped conglomerates, suggesting the same mechanism ofglomeration in both cases (HA, MO).

The EBSD analyses revealed preferential nucleation of new grains at the Zn-HA/MO interfaces (Figure 3a₁–c₁). The nucleation process could be explained by the particle stimulated nucleation process (PSN) [49]. In our case, only the mechanical connection between Zn and ceramic particles can be expected. In addition, there is a difference in the mechanical behavior of individual components (zinc behaves plastically, while the ceramics are hard and brittle). The aforementioned facts suggested that the ceramic particles transferred the stress to zinc matrix without their being damaged and caused the plastic deformation of the zinc matrix. The deformation caused by particles was localized to the closest surrounding of the ceramic conglomerates leading to an increment of dislocation density in those areas (easier nucleation). In addition, Wang et al. [50] confirmed that the presence of conglomerates in the material increases the driving force of recrystallization nucleation. Based on this, the number of nuclei should be increased in the case of the Zn-8HA sample (Figure 3c₁) [40]. Moreover, the low number of low angle boundaries and low internal stresses pointed out the same recrystallization mechanism (discontinuous dynamic recrystallization) as in our previous study concerning Zn-HA composites [40]. Because the recrystallized texture is in a relationship with the deformation texture (rotation along the c-axis of about 30° and along the <10–10> axes about 90°), the mechanisms causing the deformation during the extrusion can be suggested. The observed texture suggests that the basal and 2nd order pyramidal slip were the main deformation mechanisms during the extrusion. In the case of an ideal basal slip, only the crystallographic directions close the normals to the basal planes and (11–20) the planes can be expected in the IPFs in PD (Figure 3). Besides the basal planes, we observed also crystallographic planes slightly tilted from the basal ones, which suggests that another deformation mechanisms (twinning, prismatic or pyramidal slip) was also active during the extrusion [51]. Twinning and prismatic slip can be excluded due to the absence of twins in the material structure, or high values of critical resolved shear stress (CRSS) [52] suggesting that the basal and pyramidal slip systems made the main contribution to the deformation.

As can be seen in Figure 4, both parameters (amount and morphology of ceramic particles) significantly affected the mechanical performance of the tested materials. According to tensile and compressive measurements, the mutual relations between ceramic particles (i) composition, (ii) amount, (iii) shape and size, and resulted mechanical properties could be discussed reliably. (i) The chemical composition did not affect the mechanical properties and thus, the effect of chemical composition could be considered negligible. Both HA and MO generally consist of Ca, P, O and H, suggesting a similar contribution to mechanical properties. Our observation can be supported by Equation (4) expressing the relationship between volume fraction of ceramic reinforcement (V_A) and metal matrix (V_B) and their strengths (σ_A —strength of ceramic reinforcement, σ_B —strength of metal matrix). According to the literature [53,54], the strengths of HA and MO are approximately identical, which confirms the negligible effect of the chosen ceramic reinforcement.

$$\sigma_C = \sigma_A \cdot V_A + \sigma_B \cdot V_B \quad (4)$$

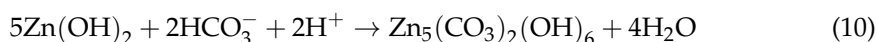
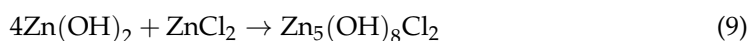
(ii) The amount of the added ceramic reinforcement had a crucial influence on the mechanical properties of zinc composites. The increasing amount of added HA led to a reduction of mechanical properties in compression and tension as well. The higher content

of globular HA particles lowers the desired synergistic effects. The probable reason for this is the increasing volume fraction of ceramic conglomerates in the zinc matrix. Such an amount of the ceramic conglomerates resulted in the high-volume fraction of hard and brittle particles, which lowers the mechanical characteristics. Furthermore, the connections between the ceramic particles and the zinc matrix had only the mechanical character. This led to the formation of defects and the amount of defects increased with the increasing content of HA.

(iii) The major differences could be found in the ductility of prepared composites. The addition of MO significantly improved ductility and this fact can be explained by the shape and size of used particles. The MO particles had a rod-like shape while HA had a globular shape. The bonds between metal matrix and ceramic particles were mechanical and their nature influenced the total adhesion between the particles and the Zn matrix. Although globular and rod-like shape particles belong among the particle-reinforced composites, the slight differences in their shape plays an important role only in ductility. The composites with globular HA particles contained many more interfaces between the individual particles and the matrix resulted in a higher adhesion and in a higher rigidity. On the other hand, the composite with the “longer” rod-like shape MO particles exhibited almost the same UTS but the ductility value was approximately two times higher. Because the Zn-MO composite was loaded in an extrusion direction, we can consider the rod-like shape MO particles acts as short “fibers”, where the stress/tension is transmitted through those fibers. For these reasons, the values of UTS are approximately the same for both prepared composites; however, the Zn-MO possessed better ductility. The Young’s modulus was determined to be approximately 55 GPa. This point to a significant decrease of the modulus in comparison to the theoretical value for pure Zn determined by Tromans et al. (110–120 GPa) [55]. The value of the composite modulus can be evaluated according to Equation (4) (with the substitution of sigma by modulus value), and the values are in good agreement with those obtained by Tromans [55]. This means that the theoretical value of the modulus should be significantly higher (two times) in comparison to the measured value. This confirmed that the ceramic particles were weakly bonded to the zinc matrix and lowers the value of Young’s modulus as a consequence. It needs to be emphasized that the decrease in the modulus value is very beneficial for applications in bone surgery. Such a decrease results in a lower risk of future failure caused by the stress shield effect and enhances the usability of those materials.

As can be seen from Table 6, the corrosion rates evaluated using weight loss and ion release were significantly different. The reason for such a difference was the predominant binding of Zn^{2+} ions into corrosion products. Based on that, only the corrosion rates evaluated by weight loss can be taken into account. The weight loss method confirmed the highest degradation rate of the Zn-4MO sample, which could be ascribed to the relatively low stability of monetite in the alkaline environments [56]. The behavior of the Zn-4MO in the initial stages of the exposition could be described according to Equations (5) and (6). As can be seen from Equation (6), the depolarization reaction led to the formation of OH^- ions and to a gradual alkalization of the solution (up to pH 8.4). This alkalization provided suitable conditions for the dissolution of the monetite to Ca^{2+} and PO_4^{3-} ions [56]. Dissolution of monetite was also confirmed by AAS, where the increased concentration of Ca^{2+} ions was found in the solution. This process frequently leads to the formation of more stable apatite (hydroxyapatite) [56]. However, the rate of this process is relatively low [56], and the process did not take place during the exposition of ZnHA/MO samples. Instead, the formation of thermodynamically less stable $ZnHPO_4$ (Equation (12) [57]) was observed by XRD suggesting the significant influence of the kinetics. It needs to be emphasized that the process mentioned above describes only the changes connected with the higher weight loss of Zn-4MO. However, the creation of simonkolleite and hydrozincite (Equation (9) [58] and Equation 10 [59]) was the main process in both cases (Zn-4HA and Zn-4MO). The process of monetite dissolution and interaction with Zn^{2+} ions could not be freely transformed into the body environment for several reasons. One of them

is homeostasis in the human body, which includes a pH regulation system. In human skeletal muscles, pH values range from 7.2 to 7.4 [60]. This means that the conditions for such a transformation could not be reached. The second reason is the kinetics of reactions themselves. It is well known that the ions released due to dissolution of monetite can interact with cells and enhance their viability (concentration dependence) [54]. Based on this, in vitro and in vivo tests should be done to confirm the presented mechanism. Despite the unverified mechanism, the MO seems to be a more suitable reinforcement for biodegradable applications than HA.



5. Conclusions

The preparation of the Zn-based composites reinforced with ceramic components (HA, MO) and their influence onto mechanical and corrosion properties has been reported in the present manuscript. The main findings can be drawn from the following points:

- i. HA and MO formed spherical conglomerates in the extruded materials due to their physical characteristics. The conglomerates created, with the Zn matrix, only the mechanical connection, which had an influence on the resulting properties of the materials.
- ii. The influence of the amount and morphology of the particles on the mechanical properties was found. The higher content of the ceramic particles resulted in the lower amount of interconnections between individual zinc particles, decreasing the material strength approximately by 40–60 MPa. In addition, the morphology of ceramic particles affected predominantly the ductility of the materials. More precisely, the presence of rod-like particles increased the ductility of the material by 100% (from 2.1 to 5.1%) compared with the globular one.
- iii. The type of reinforcement affected the corrosion behavior. The measurements pointed to a higher degradation rate of the Zn-4MO sample due to the gradual dissolving of the MO. The process characterizes a minor part of material degradation and explains the differences between Zn-4HA and Zn-4MO corrosion rates (0.1 mm/a). Exposure to a corrosive environment results in the formation of corrosion products, primarily hydrozincite, simonkolleite and zinc hydrogen phosphate.

Material characterization revealed the ideal behavior of Zn-4MO composites for biodegradable applications. Based on the literature, such behavior was observed in the case of Zn-apatite composites for the first time and revealed possible manners by which to enhance the usability of these composite materials.

Author Contributions: K.H.: Formal analysis, Investigation; J.P.: Conceptualization, Investigation, Project administration, Writing—original draft; A.Š.: Writing—original draft, Writing—review and editing; V.B.: Conceptualization, Investigation; P.V.: Investigation, Formal analysis; T.Š.: Investigation, Formal analysis; D.V.: Supervision, F.P.: Investigation, J.Č.: Writing—review and editing. All authors have read and agreed to the published version of the manuscript.

Funding: This research was funded by Czech Science Foundation, grant number 18-06110S, specific university research—grant A2_FCFT_2020_039, Operational Program Research, Development and Education financed by European Structural and Investment Funds and the Czech Ministry of Education, Youth and Sports (Project No. SOLID21-CZ.02.1.01/0.0/0.0/16_019/0000760) and by the LNSM Research Infrastructure supported by MEYS CR (LM2018110).

Institutional Review Board Statement: Not applicable.

Informed Consent Statement: Not applicable.

Data Availability Statement: The raw/processed data will be provided as request.

Acknowledgments: The authors would also like to thanks to Orsolya Molnárová for EBSD analyzing.

Conflicts of Interest: The authors declare no conflict of interest.

References

- Levy, G.K.; Goldman, J.; Aghion, E. The Prospects of Zinc as a Structural Material for Biodegradable Implants—A Review Paper. *Metals* **2017**, *7*, 402. [[CrossRef](#)]
- Li, Y.; Pavanram, P.; Zhou, J.; Lietaert, K.; Taheri, P.; Li, W.; San, H.; Leeftang, M.; Mol, J.; Jahr, H.; et al. Additively manufactured biodegradable porous zinc. *Acta Biomater.* **2020**, *101*, 609–623. [[CrossRef](#)] [[PubMed](#)]
- Drelich, A.J.; Zhao, S.; Guillory, R.J.; Drelich, J.W.; Goldman, J. Long-term surveillance of zinc implant in murine artery: Surprisingly steady biocorrosion rate. *Acta Biomater.* **2017**, *58*, 539–549. [[CrossRef](#)] [[PubMed](#)]
- Godavitarne, C.; Robertson, A.; Peters, J.; Rogers, B. Biodegradable materials. *Orthop. Trauma* **2017**, *31*, 316–320. [[CrossRef](#)]
- Li, H.; Zheng, Y.; Qin, L. Progress of biodegradable metals. *Prog. Nat. Sci.* **2014**, *24*, 414–422. [[CrossRef](#)]
- Tan, L.; Yu, X.; Wan, P.; Yang, K. Biodegradable Materials for Bone Repairs: A Review. *J. Mater. Sci. Technol.* **2013**, *29*, 503–513. [[CrossRef](#)]
- Obayi, C.S.; Tolouei, R.; Paternoster, C.; Turgeon, S.; Okorie, B.A.; Obikwelu, D.O.; Cassar, G.; Buhagiar, J.; Mantovani, D. Influence of cross-rolling on the micro-texture and biodegradation of pure iron as biodegradable material for medical implants. *Acta Biomater.* **2015**, *17*, 68–77. [[CrossRef](#)]
- Wegener, B.; Sievers, B.; Utzschneider, S.; Müller, P.; Jansson, V.; Röfler, S.; Nies, B.; Stephani, G.; Kieback, B.; Quadbeck, P. Microstructure, cytotoxicity and corrosion of powder-metallurgical iron alloys for biodegradable bone replacement materials. *Mater. Sci. Eng. B* **2011**, *176*, 1789–1796. [[CrossRef](#)]
- Chen, Y.; Xu, Z.; Smith, C.; Sankar, J. Recent advances on the development of magnesium alloys for biodegradable implants. *Acta Biomater.* **2014**, *10*, 4561–4573. [[CrossRef](#)]
- Gu, X.-N.; Zheng, Y.-F. A review on magnesium alloys as biodegradable materials. *Front. Mater. Sci. China* **2010**, *4*, 111–115. [[CrossRef](#)]
- Vojtěch, D.; Kubásek, J.; Šerák, J.; Novák, P. Mechanical and corrosion properties of newly developed biodegradable Zn-based alloys for bone fixation. *Acta Biomater.* **2011**, *7*, 3515–3522. [[CrossRef](#)]
- Kubásek, J.; Vojtěch, D.; Jablonská, E.; Pospíšilová, I.; Lipov, J.; Ruml, T. Structure, mechanical characteristics and in vitro degradation, cytotoxicity, genotoxicity and mutagenicity of novel biodegradable Zn–Mg alloys. *Mater. Sci. Eng. C* **2016**, *58*, 24–35. [[CrossRef](#)]
- Yang, Y.; Cheng, Y.; Peng, S.; Xu, L.; He, C.; Qi, F.; Zhao, M.; Shuai, C. Microstructure evolution and texture tailoring of reduced graphene oxide reinforced Zn scaffold. *Bioact. Mater.* **2021**, *6*, 1230–1241. [[CrossRef](#)] [[PubMed](#)]
- Su, Y.; Cockerill, I.; Wang, Y.; Qin, Y.-X.; Chang, L.; Zheng, Y.; Zhu, D. Zinc-Based Biomaterials for Regeneration and Therapy. *Trends Biotechnol.* **2019**, *37*, 428–441. [[CrossRef](#)] [[PubMed](#)]
- Kabir, H.; Munir, K.; Wen, C.; Li, Y. Recent research and progress of biodegradable zinc alloys and composites for biomedical applications: Biomechanical and biocorrosion perspectives. *Bioact. Mater.* **2021**, *6*, 836–879. [[CrossRef](#)]
- Liu, Y.; Lu, B.; Cai, Z. Recent Progress on Mg- and Zn-Based Alloys for Biodegradable Vascular Stent Applications. *J. Nanomater.* **2019**, *2019*, 1–16. [[CrossRef](#)]
- Vojtěch, D.; KUBÁSEK, J.; Čapek, J. Comparative mechanical and corrosion studies on magnesium, zinc and iron alloys as biodegradable metals. *Mater. Tehnol.* **2015**, *49*, 877–882. [[CrossRef](#)]
- Liu, L.; Meng, Y.; Dong, C.; Yan, Y.; Volinsky, A.A.; Wang, L.-N. Initial formation of corrosion products on pure zinc in simulated body fluid. *J. Mater. Sci. Technol.* **2018**, *34*, 2271–2282. [[CrossRef](#)]
- Jia, B.; Yang, H.; Zhang, Z.; Qu, X.; Jia, X.; Wu, Q.; Han, Y.; Zheng, Y.; Dai, K. Biodegradable Zn–Sr alloy for bone regeneration in rat femoral condyle defect model: In vitro and in vivo studies. *Bioact. Mater.* **2021**, *6*, 1588–1604. [[CrossRef](#)]
- Jia, B.; Yang, H.; Han, Y.; Zhang, Z.; Qu, X.; Zhuang, Y.; Wu, Q.; Zheng, Y.; Dai, K. In vitro and in vivo studies of Zn–Mn biodegradable metals designed for orthopedic applications. *Acta Biomater.* **2020**, *108*, 358–372. [[CrossRef](#)]
- Li, Z.; Shi, Z.-Z.; Hao, Y.; Li, H.-F.; Zhang, H.-J.; Liu, X.-F.; Wang, L.-N. Insight into role and mechanism of Li on the key aspects of biodegradable Zn Li alloys: Microstructure evolution, mechanical properties, corrosion behavior and cytotoxicity. *Mater. Sci. Eng. C* **2020**, *114*, 111049. [[CrossRef](#)]

22. Gong, H.; Wang, K.; Strich, R.; Zhou, J.G. In vitro biodegradation behavior, mechanical properties, and cytotoxicity of biodegradable Zn-Mg alloy. *J. Biomed. Mater. Res. Part B Appl. Biomater.* **2015**, *103*, 1632–1640. [CrossRef]
23. Shi, Z.-Z.; Gao, X.-X.; Chen, H.-T.; Liu, X.-F.; Li, A.; Zhang, H.-J.; Wang, L.-N. Enhancement in mechanical and corrosion resistance properties of a biodegradable Zn-Fe alloy through second phase refinement. *Mater. Sci. Eng. C* **2020**, *116*, 111197. [CrossRef]
24. Xie, Y.; Zhao, L.; Zhang, Z.; Wang, X.; Wang, R.; Cui, C. Fabrication and properties of porous Zn-Ag alloy scaffolds as biodegradable materials. *Mater. Chem. Phys.* **2018**, *219*, 433–443. [CrossRef]
25. Čapek, J.; KUBÁSEK, J.; Pinc, J.; Maňák, J.; Molnárová, O.; Drahekoupil, J.; Čavojský, M. ZnMg0.8Ca0.2 (wt%) biodegradable alloy—The influence of thermal treatment and extrusion on microstructural and mechanical characteristics. *Mater. Charact.* **2020**, *162*, 110230. [CrossRef]
26. Čapek, J.; Pinc, J.; Kubásek, J.; Molnárová, O.; Maňák, J.; Drahekoupil, J. ZnMg0.8Ca/Sr0.2 ternary alloys—The influence of the third element on material properties. *Procedia Struct. Integr.* **2019**, *23*, 3–8. [CrossRef]
27. Venezuela, J.; Dargusch, M. The influence of alloying and fabrication techniques on the mechanical properties, biodegradability and biocompatibility of zinc: A comprehensive review. *Acta Biomater.* **2019**, *87*, 1–40. [CrossRef] [PubMed]
28. Shi, Z.-Z.; Li, Z.-L.; Bai, W.-S.; Tuoliken, A.; Yu, J.; Liu, X.-F. (Fe, Mn)Zn13 phase and its core-shell structure in novel biodegradable Zn-Mn-Fe alloys. *Mater. Des.* **2019**, *162*, 235–245. [CrossRef]
29. Shi, Z.-Z.; Yu, J.; Liu, X.-F.; Zhang, H.-J.; Zhang, D.-W.; Yin, Y.-X.; Wang, L.-N. Effects of Ag, Cu or Ca addition on microstructure and comprehensive properties of biodegradable Zn-0.8Mn alloy. *Mater. Sci. Eng. C* **2019**, *99*, 969–978. [CrossRef] [PubMed]
30. Zhu, D.; Cockerill, I.; Su, Y.; Zhang, Z.; Fu, J.; Lee, K.-W.; Ma, J.; Okpokwasili, C.; Tang, L.; Zheng, Y.; et al. Mechanical Strength, Biodegradation, and in Vitro and in Vivo Biocompatibility of Zn Biomaterials. *ACS Appl. Mater. Interfaces* **2019**, *11*, 6809–6819. [CrossRef] [PubMed]
31. Wang, L.; Luo, Q.; Zhang, X.; Qiu, J.; Qian, S.; Liu, X. Co-implantation of magnesium and zinc ions into titanium regulates the behaviors of human gingival fibroblasts. *Bioact. Mater.* **2021**, *6*, 64–74. [CrossRef] [PubMed]
32. Ratha, I.; Datta, P.; Balla, V.K.; Nandi, S.K.; Kundu, B. Effect of doping in hydroxyapatite as coating material on biomedical implants by plasma spraying method: A review. *Ceram. Int.* **2021**, *47*, 4426–4445. [CrossRef]
33. Foltz, J.V.; Blackmon, C.M. Metal-Matrix Composites. 2013. Available online: <http://hdl.handle.net/11115/214> (accessed on 16 March 2021).
34. Witte, F.; Feyerabend, F.; Maier, P.; Fischer, J.; Störmer, M.; Blawert, C.; Dietzel, W.; Hort, N. Biodegradable magnesium-hydroxyapatite metal matrix composites. *Biomaterials* **2007**, *28*, 2163–2174. [CrossRef]
35. Yin, X.; Calderin, L.; Stott, M.J.; Sayer, M. Density functional study of structural, electronic and vibrational properties of mg- and zn-doped tricalcium phosphate biomaterials. *Biomaterials* **2002**, *23*, 4155–4163. [CrossRef]
36. Fujii, E.; Ohkubo, M.; Tsuru, K.; Hayakawa, S.; Osaka, A.; Kawabata, K.; Bonhomme, C.; Babonneau, F. Selective protein adsorption property and characterization of nano-crystalline zinc-containing hydroxyapatite. *Acta Biomater.* **2006**, *2*, 69–74. [CrossRef]
37. Mensah-Darkwa, K.; Gupta, R.; Kumar, D. Mechanical and Corrosion Properties of Magnesium-Hydroxyapatite (Mg-HA) Composite Thin Films. *J. Mater. Sci. Technol.* **2013**, *29*, 788–794. [CrossRef]
38. Gu, X.; Zhou, W.; Zheng, Y.; Dong, L.; Xi, Y.; Chai, D. Microstructure, mechanical property, bio-corrosion and cytotoxicity evaluations of Mg/HA composites. *Mater. Sci. Eng. C* **2010**, *30*, 827–832. [CrossRef]
39. Yang, H.; Qu, X.; Lin, W.; Wang, C.; Zhu, D.; Dai, K.; Zheng, Y. In vitro and in vivo studies on zinc-hydroxyapatite composites as novel biodegradable metal matrix composite for orthopedic applications. *Acta Biomater.* **2018**, *71*, 200–214. [CrossRef]
40. Pinc, J.; Čapek, J.; Hybášek, V.; Průša, F.; Hosová, K.; Maňák, J.; Vojtěch, D. Characterization of Newly Developed Zinc Composite with the Content of 8 wt.% of Hydroxyapatite Particles Processed by Extrusion. *Materials* **2020**, *13*, 1716. [CrossRef]
41. Pathak, D.K.; Pandey, P.M. Evaluation of in vitro corrosion behavior of zinc-hydroxyapatite and zinc-hydroxyapatite-iron as biodegradable composites. *J. Biomed. Mater. Res. Part B Appl. Biomater.* **2021**, *109*, 436–450. [CrossRef]
42. Pinc, J.; Čapek, J.; KUBÁSEK, J.; Průša, F.; Hybášek, V.; Vejtát, P.; Sedlářová, I.; Vojtěch, D. Characterization of a Zn-Ca5(PO4)3(OH) Composite with a High Content of the Hydroxyapatite Particles Prepared by the Spark Plasma Sintering Process. *Metals* **2020**, *10*, 372. [CrossRef]
43. Nawang, R.; Hussein, M.Z.; Matori, K.A.; Abdullah, C.A.C.; Hashim, M. Physicochemical properties of hydroxyapatite/montmorillonite nanocomposite prepared by powder sintering. *Results Phys.* **2019**, *15*, 102540. [CrossRef]
44. Švecová, M.; Bartůněk, V. Facile synthesis of monetite nanoparticles from basic raw materials. *Ceram. Int.* **2018**, *44*, 16079–16082. [CrossRef]
45. Liu, L.; Gebresellasi, K.; Collins, B.; Zhang, H.; Xu, Z.; Sankar, J.; Lee, Y.-C.; Yun, Y. Degradation Rates of Pure Zinc, Magnesium, and Magnesium Alloys Measured by Volume Loss, Mass Loss, and Hydrogen Evolution. *Appl. Sci.* **2018**, *8*, 1459. [CrossRef]
46. Müller, L.; Müller, F.A. Preparation of SBF with different HCO₃⁻ content and its influence on the composition of biomimetic apatites. *Acta Biomater.* **2006**, *2*, 181–189. [CrossRef]
47. Levoguer, C. Using laser diffraction to measure particle size and distribution. *Met. Powder Rep.* **2013**, *68*, 15–18. [CrossRef]
48. Bystrov, V.S.; Paramonova, E.; Dekhtyar, Y.; Katashev, A.; Karlov, A.; Polyaka, N.; Bystrova, A.V.; Patmalnieks, A.; Kholkin, A.L. Computational and experimental studies of size and shape related physical properties of hydroxyapatite nanoparticles. *J. Phys. Condens. Matter* **2011**, *23*, 065302. [CrossRef]

49. Robson, J.; Henry, D.; Davis, B. Particle effects on recrystallization in magnesium–manganese alloys: Particle-stimulated nucleation. *Acta Mater.* **2009**, *57*, 2739–2747. [[CrossRef](#)]
50. Wang, X.; Hu, X.; Nie, K.; Deng, K.; Wu, K.; Zheng, M. Dynamic recrystallization behavior of particle reinforced Mg matrix composites fabricated by stir casting. *Mater. Sci. Eng. A* **2012**, *545*, 38–43. [[CrossRef](#)]
51. Wang, Y.; Huang, J. Texture analysis in hexagonal materials. *Mater. Chem. Phys.* **2003**, *81*, 11–26. [[CrossRef](#)]
52. Solas, D.E.; Tomé, C.N.; Engler, O.; Wenk, H.R. Deformation and recrystallization of hexagonal metals: Modeling and experimental results for zinc. *Acta Mater.* **2001**, *49*, 3791–3801. [[CrossRef](#)]
53. Laasri, S.; Taha, M.; Hajjaji, A.; Laghzizil, A.; Hlil, E. Mechanical properties of calcium phosphate biomaterials. *Mol. Cryst. Liq. Cryst.* **2016**, *628*, 198–203. [[CrossRef](#)]
54. Tamimi, F.; Sheikh, Z.; Barralet, J. Dicalcium phosphate cements: Brushite and monetite. *Acta Biomater.* **2012**, *8*, 474–487. [[CrossRef](#)]
55. Tromans, D. Elastic Anisotropy of HCP Metal Crystals and Polycrystals. *Int. J. Res. Rev. Appl. Sci.* **2011**, *6*, 462–483.
56. Da Silva, M.P.; Lima, J.; Soares, G.; Elias, C.; De Andrade, M.; Best, S.; Gibson, I. Transformation of monetite to hydroxyapatite in bioactive coatings on titanium. *Surf. Coatings Technol.* **2001**, *137*, 270–276. [[CrossRef](#)]
57. Huang, Y.; Zhang, X.; Qiao, H.; Hao, M.; Zhang, H.; Xu, Z.; Zhang, X.; Pang, X.; Lin, H. Corrosion resistance and cytocompatibility studies of zinc-doped fluorohydroxyapatite nanocomposite coatings on titanium implant. *Ceram. Int.* **2016**, *42*, 1903–1915. [[CrossRef](#)]
58. Zhang, Y.; Yan, Y.; Xu, X.; Lu, Y.; Chen, L.; Li, D.; Dai, Y.; Kang, Y.; Yu, K. Investigation on the microstructure, mechanical properties, in vitro degradation behavior and biocompatibility of newly developed Zn-0.8%Li-(Mg, Ag) alloys for guided bone regeneration. *Mater. Sci. Eng. C* **2019**, *99*, 1021–1034. [[CrossRef](#)] [[PubMed](#)]
59. Liu, X.; Yang, H.; Xiong, P.; Li, W.; Huang, H.-H.; Zheng, Y. Comparative studies of Tris-HCl, HEPES and NaHCO₃/CO₂ buffer systems on the biodegradation behaviour of pure Zn in NaCl and SBF solutions. *Corros. Sci.* **2019**, *157*, 205–219. [[CrossRef](#)]
60. Juel, C. Regulation of pH in human skeletal muscle: Adaptations to physical activity. *Acta Physiol.* **2008**, *193*, 17–24. [[CrossRef](#)] [[PubMed](#)]